# Analysis of particle-laden fluid flows, tortuosity and particle-fluid behaviour in metal foam heat exchangers

Sahan T.W. Kuruneru [a,*], Emilie Sauret [a,*], Kambiz Vafai [b], Suvash C. Saha [a], YuanTong Gu [a]

[a] Laboratory for Advanced Modelling and Simulation in Engineering and Science, School of Chemistry, Physics & Mechanical Engineering, Queensland University of Technology, Brisbane, QLD 4001, Australia
[b] Mechanical Engineering Department, University of California, Riverside, CA 93210, USA

## HIGHLIGHTS

- A coupled FVM-DEM method to examine mass transfer and fouling in porous media.
- Compared numerical and analytical pressure drop results.
- Quantitative analysis of tortuosity and solid-gas behaviour.
- Fluid resistance dependent on particle properties and Reynolds number.

## ARTICLE INFO

## ABSTRACT

Tortuosity and porosity are critical parameters for characterizing fluid flow in porous media. These parameters are of paramount importance in the design of porous compact heat exchangers, packed bed reactors, and catalysis supports; however, in the context of heat exchangers, these parameters are generally formulated for single-phase fluid flow under steady-state conditions. However, most industrial flows in a porous medium such as metal foams comprise of transient particle-laden fluid flow. A coupled finite volume and discrete element method (FVM-DEM) is developed to examine transient particle-laden Stokesian flow, particulate fouling (deposition), and fluid flow patterns in an idealized porous metal foam. This work presents a comparative analysis of the analytical and numerical pressure drop profiles. The solid-gas suspension in a porous media is discussed. Secondly, a new time-dependent pore-level fluid tortuosity relation is established which is linked with a modified porosity-based Darcy-Forchheimer equation. Fluid disturbance attributable to the inception of particle deposition is quantified by the tortuosity and instantaneous shift in streamline angle ratio. It is shown that the streamline angle ratio and the meandering of fluid flow paths vary with changing porosity and tortuosity. Moreover, the Reynolds number and particle density play a critical role in the alteration of the resistance to fluid flow and permeability which is related to the tortuosity and variation in fluid flow behaviour. The results and numerical method serves as a steppingstone to better optimize various heat exchangers while taking into account complex multiphase flow behaviour and the tortuous flow paths of porous structures.

© 2017 Elsevier Ltd. All rights reserved.

## 1. Introduction

### 1.1. Single phase fluid flow in porous metal foams

Metal foams are a class of highly porous materials that exhibit unique thermo-physical properties such as high specific surface, high thermal conductivity, low density, superior interfacial heat transfer, favourable thermal and corrosion resistance, and high

* Corresponding authors.
   E-mail addresses: sahantw@gmail.com (S.T.W. Kuruneru), emilie.sauret@qut.edu.au (E. Sauret).

permeability (Han et al., 2012). Research has shown that the fluid tortuosity, expressed as a reciprocal of the square root of the porosity (Bruggeman, 1935), of an aluminium foam is found to be greater than 1 (Onstad et al., 2011). This result signifies that metal foams have a strong propensity to accentuate fluid mixing and turbulence, which is arguably linked to the stochastic orientation of these highly porous structures. There is a wealth of literature describing metal foams immersed in a single-phase incompressible fluid. Kopanidis et al. (2010) detailed fluid behaviour through the pores of a metal foam and concluded that specific regions of the flow allowed unperturbed flow through the pores, whereas winding of the flow streamlines is observed in other regions. Dukhan

(2012) analytically obtained the solution to the Brinkman-Darcy equation by comparing it with the Bessel function. The average fluid velocity in the foam was found to be approximately equal to the free stream velocity for low Darcy numbers as the velocity is invariant throughout most of the structure. Onstad et al. (2011) used streamline displacement analysis in combination with some post-processing with the use of an adaptive trapezoidal integration algorithm of the velocity field through an open-cell metal foam. It was found that, at a cell Reynolds number of 840, the transverse fluid velocity is about 20% greater than the superficial velocity passing through the foam. However, there exists no relationship between the transverse mechanical mixing and tortuosity. Matsumura et al. (2015) used ensemble averaging to account for the effects of porosity and Reynolds number on the mean permeability and tortuosity for fluid flow through *random* packs of immobile ellipses. The ellipse aspect ratio has a strong effect on the tortuosity. It is also found that the Carman-Kozeny factor (Happel and Brenner, 1973) is not constant but depends largely on the porosity and aspect ratio. Coletti et al. (2014) studied fluid flow and scalar transport in lotus-type porous metals. The random orientation of porous metals produces a significant mechanical dispersion effect which results in the time mean fluid streamlines to meander in a random-walk manner (*i.e.* mechanical mixing). It was inferred that the diffusivity coefficient associated with mechanical dispersion is several times greater than the fluid molecular diffusivity at higher Reynolds numbers.

The unique properties of metal foams make it a viable material for various applications such as compact heat exchangers (Han et al., 2012), heat sinks (Bayomy et al., 2016), condensers (T'Joen et al., 2010), tubular reactors (Hutter et al., 2011) and catalyst supports in fixed-bed reactors (Giani et al., 2005). Many studies have examined the efficacy of porous metal foam inserts for various heat exchanger applications for the process and power generation industries. Dixit and Ghosh (2016) experimentally examined thermo-hydraulic behaviour of copper foams with various pore densities and concluded that the air entering the foam at uniform temperature exits with a spatial temperature variation. Mancin et al. (2012) provided a comprehensive analysis of heat transfer coefficient, permeability, and pressure drop profiles through copper (Cu) foams of various porosities, number of pores per inch (PPI), air mass flow rates, and three different heat fluxes. It was found that the Cu-40-6.6 (40 PPI; 6.6% relative density) exhibits about 10% lower global heat transfer coefficient than the Cu-5-6.7 (5 PPI) sample. For all the samples, the mean wall temperature monotonically decreases with increasing pumping fluid power, and Cu-10-9.5 exhibits the lowest mean wall temperature whereas Cu-20-6.7 and Cu-40-6.6 exhibit identical heat transfer performance. Chen et al. (2015) numerically examined the performance of a double pipe heat exchanger with and without metal foam inserts. A major finding is that the performance factor can increase by more than 700% albeit a high pressure drop is realised. Moreover, the overall heat transfer performance increases by a factor of 18; however, the effects of metal foams on heat transfer diminishes for Reynolds number commencing about 1000. Shell-and-tube heat exchangers (STHXs) are commonly found in chemical and petrochemical plants. Zhang et al. (2009) examined the performance of STHXs with helical (STHXsHB) and segmented baffles (STHXsSB) of various helix angles. It was found that heat exchanger with helical baffles of 40° exhibit the highest performance among the five STHXs tested. The authors emphasized that additional techniques are required to further increase the heat transfer performance. Metal foams have the potential to achieve that. In fact, Rad et al. (2015) found that the inclusion of metal foam inserts in STHXs yield improvements in the heat transfer although a higher pressure drop is realised. Sauret and Hooman (2014) used Eulerian-Lagrangian method to predict regions of particle deposition in idealized porous metal foam heat exchangers. In this paradigm, discrete granular system dynamics and the interphasial interaction between the particles and wall-bounded Stokesian flow has been neglected. Zafari et al. (2015) conducted a microtomography-based numerical simulation of fluid flow and heat transfer in open-cell metal foams. The findings divulge that a temperature gradient attenuates the air density inside the foam, which in turn increases the fluid flow velocity. Moreover, an increase in the superficial inlet velocity yields an increase in the local and average convection coefficient in the metal foam. Yang et al. (2012) investigated the heat transfer performance and effectiveness of an aluminium-foam inserted in a tube in two different configurations: the first configuration consists of a tube with its wall covered with a porous medium layer, the second configuration is based on a tube with a porous medium core. It was found that, under an equal low range pumping power, the heat transfer performance of the second configuration is higher than the first, whereas in an equal high range pumping power, the first configuration is superior to the second in terms of thermal performance. Hooman et al. (2012) studied the impact of fouling on the thermohydraulic performance of an idealized metal foam exchanger in the form of a simple cubic unit cell. This idealized metal foam structure is an approximate representation of the real metal foam structure of Bhattacharya et al., 2002. It was found that a 15% decrease in the heat transfer from the heated surface is prediction. However, their study assumes uniform particulate deposition layer which, in reality, is not valid as fouling is inherently transient and unsteady in nature. Secondly, impact of the foulant on the carrier fluid has not been investigated.

The major weakness of all of the above cited publications is that the studies rationalised non-trivial heat transfer and pressure drop characteristics of porous metal foams. The limitation of the mathematical models in these publications stems from the basic assumption that the global quantitates, such as the pressure drop, and temperature distribution, are *not* based on transient dense multiphase flows which is the norm in many environmental and industrial applications (Tian et al., 2007; Traore et al., 2015; Tryggvason, 2010). The preceding literature review is purely based on single-phase flows; however, there are many existing studies on multiphase flow. However, these multiphase studies use numerical methods that are based on assumptions such as point particle (zero particle volume) method [Dritselis, 2017; Yao and Fairweather, 2012] where dilute flows is assumed, and particle-particle (interparticle) and particle-wall collisions were not taken into account. Other assumptions include the use of the Two Fluid Model (TFM) or Eulerian-Eulerian (EE) method to study solid-gas flows in fluidized beds and pneumatic conveying bends, among others (Lee et al., 2004; Lu et al., 2011; Vepsalainen et al., 2014; Yusuf et al., 2011); however, this method considers the solid phase as an interpenetrating continua like the gas phase which will not yield accurate descriptors, namely, the position, velocity, and energy of solids, of the solid phase in wall-bounded dense solid-gas particulate systems. The Eulerian description of particle deposition in specific industrial applications has the numerical advantages of speed and efficiency. Ni et al. (2014) have shown that the results from the Eulerian particle deposition model are in good agreement with the experimental results. Although the TFM to model solid-gas flows incurs substantially lower computational cost than the Eulerian-Lagrangian (EL) method, the EE method does not yield detailed particle motion description; additionally, numerical issues are encountered in poly- and multi-disperse particulate systems with particles of different sizes and shapes (Zhong et al., 2016). Indeed, the point-particle method cannot capture experimentally observed turbulence attenuation (Eaton, 2009); what is more, fully resolved simulations such as inter-particle, particle-wall, particle-fluid interactions clearly highlight the significance of local flow around particles (Eaton, 2009).

Population balance methods (PBM) coupled with CFD are used to *predict* the agglomeration, deposition, and fouling of hydrates in industrial pipelines with hydrate-laden liquid flows (Balakin et al., 2011, 2016). PBMs yield reasonably accurate predictions such as agglomerate size distributions but the *actual* micromechanics and microstructure of these aggregates or interactions between various aggregates and wall-bounded immersed surfaces cannot be captured and fully resolved (Marshall, 2009). In other words, these major assumptions misjudge the actual inter-particle/particle-particle, particle-wall and particle-fluid transport behaviour in dense solid-gas flows in porous media. Furthermore, wall-proximity effect on the particle-fluid motion is indistinct. Therefore, it remains to be seen whether an identical heat exchanger performance, such as pressure drop, heat transfer performance, and the actual solid-gas flow characteristics is observed in the presence of multiphase flows (*i.e.* solid-gas flows and foulants or any form of particulate foulant adhering to the fluid-saturated metal foam). It is noteworthy that a robust numerical model is of paramount importance to unravel complex solid-gas flows as a means to mitigate particulate fouling in a plethora of engineering applications such as compact heat exchangers, heat sinks for electronics cooling, coal-fired utility boilers, plate heat exchangers in food industry, and membranes bioreactors.

### 1.2. Tortuosity and particle-fluid behaviour

Multiphase transport in porous media can erode or deposit material thereby changing the path of fluid flow and attenuating fluid flow resistance. This will inadvertently compromise the performance of metal foam heat exchangers. To the best of the authors' knowledge, the study of the tortuosity of a porous network and the fluid characteristics under unsteady multiphase flow conditions for heat exchanger applications has not been reported in the literature. The effect of wall-bounded Stokesian fluid and particle deposits on the topology of the fluid streamlines and tortuosity is indistinct. Tortuosity is one such complex variable which is used to obtain transport properties such as effective conductivity and effective diffusivity of porous electrodes in lithium-ion (Li-ion) batteries (Thorat et al., 2009). The MacMullin number (MacMullin and Muccini, 1956), expressed as a ratio of the tortuosity to porosity, is used to predict the effective conductivity or diffusive resistance in separators and porous electrodes as a means to optimize li-ion batteries. Both porosity and tortuosity could be used to characterize thermo-fluidic properties of porous aluminium foam anodes in direct coal fuel cells (DCFC). The relation of tortuosity is seen as an important parameter to quantify the diffusion coefficient of the diffusing species in porous catalyst pellets (Ghanbarian et al., 2013). Precise knowledge of the porosity, tortuosity, and the usual coefficient of diffusion of reactives inside catalytic pellets is essential in the design of trickle-bed reactors (Midoux and Charpentier, 1973). However, the bulk of the literature on tortuosity and its relevance to thermo-fluidic properties such as diffusive resistivity is limited to power sources applications such as batteries. Nonetheless, there are several tortuosity studies of direct relevance to the chemical engineering arena such as packed beds, where the tortuosity, albeit difficult to obtain accurate values, distinctly characterises the packing structure and media homogeneity of uniform/non-uniform packed bed of spheres or complicated internal architecture of porous metal foams (Lanfrey et al., 2010; Ahmed et al., 2011). Again, these are restricted to steady single phase flows.

Tortuosity is used in describing diffusion, conduction, and fluid flow in porous configurations (Ahmed et al., 2011). The tortuosity coefficient, expressed as a square of the tortuosity, is used to estimate the Fanning friction factor and the heat transfer coefficient of a cross corrugated chevron-type plate heat exchanger (PHE) (Fernandes et al., 2007) albeit only single-phase flow was considered. Kuruneru et al. (2016) numerically examined particle-laden gas flows and particulate fouling in an idealized metal foam structure for compact heat exchangers. The bulk of the discussion is focused primarily on particulate fouling distributions in the metal foam, together with the characteristics of solid particle deposition in specific regions of the foam structure. There exist no indepth analysis of the solid-gas flow behaviour and fluid flow patterns in these porous structures. Carman (1956) defined tortuosity as the waviness of a path in a porous media; however, in the context of metal foam heat exchangers, one must be cognizant that the constrictivity of pores together with unsteady sediment transport and multiphase solid-gas, which further obscures the pores of a porous media, must be taken into account by means of an effective tortuosity and effective porosity relation. Therefore, in this study, in addition to the analysis of particle-laden gas transport and particle deposition in porous media, the porosity, tortuosity, streamlines, and solid–gas behaviour are quantified and used to characterize resistance to fluid flow in porous metal foam heat exchangers in the presence of unsteady multiphase particle-laden fluid flows.

### 1.3. Objectives

Numerically resolving the dynamical evolution of particle-particle and particle-wall interactions (four-way coupling), and particle-fluid interactions (two-way coupling) in porous media is a challenging task and prohibitively expensive. An efficient and robust numerical strategy is essential to decipher the underlying mechanisms of particle-fluid transport, particulate fouling (particle deposition), and fluid streamline patterns in porous aluminium foams. This can be achieved with the use of a coupled finite-volume and discrete element method (FVM-DEM) or a coupled Lattice Boltzmann and discrete element method (LBM-DEM). Several studies have harnessed LBM-DEM to examine complex particle suspensions and solid-gas flows (Han and Cundall, 2013; Leonardi et al., 2013, 2016; Zeiser, 2002); however, LBM incurs a significantly higher computational cost than the traditional FVM method (Tong and He, 2015). Zeiser (2002) compared the numerical accuracy of both FVM and LBM codes (single-phase flow) in simple porous medium and both methods yield identical solutions. Multi-grid or algebraic multi-grid methods which are omnipresent in FVMs damp out low-frequency oscillations and are normally applied with complex geometries. Implementing turbulence modelling and various boundary conditions could be an issue. LBM is relatively young, and simulating thermal simulations is not straightforward; moreover, there is a limit in the range of densities and viscosities in multiphase and multicomponent simulations (Kruger et al., 2017), and the difficulty in capturing solid-gas interactions in micro-gaseous flows. Developments of the LBM are still needed in order to become competitive with FV schemes (Zeiser, 2002).

In this study, a FVM-DEM is developed and implemented to study dense solid-gas (multiphase) transport and particle deposition (particulate fouling) in an idealized metal foam structure at the pore level which is discussed in Section 2. Secondly, Section 3.1 covers a qualitative analysis of the particle-fluid and particle deposition characteristics coupled with analytical validation. Finally, the fluid tortuosity, meandering of fluid paths and streamlines under transient multiphase flow conditions is quantified in Section 3.2.

## 2. Computational method

### 2.1. Governing equations and numerical implementation

In this study, the transport of incompressible air ($\rho_f$ = 1.225 kg/m$^3$) in a porous structure laden with rigid particles is modelled by the FVM-DEM method. The method accounts for fully resolved

interactions between the solid, gas, and walls of the domain. The Navier Stokes equations that govern the transport of incompressible air flow in porous systems at the pore level (Narsilio et al., 2009) are based on Eqs. (1) and (2), where $\alpha_d$ is the volume fraction occupied by the fluid, fluid velocity $v$, fluid density $\rho_f$, fluid pressure $p$, viscous stress tensor for the fluid phase $\tau$, particle-fluid interaction force $F_{pf}$, gravitational acceleration $g$:

$$\frac{\partial \alpha_d}{\partial t} + \nabla \cdot (\alpha_d \boldsymbol{v}) = 0 \tag{1}$$

$$\frac{\partial (\rho_f \alpha_d \boldsymbol{v})}{\partial t} + \nabla \cdot (\rho_f \alpha_d \boldsymbol{v}\boldsymbol{v}) = -\nabla(\alpha_d p) + \boldsymbol{F_{pf}} + \nabla \cdot (\alpha_d \tau) + \rho_f \alpha_d \boldsymbol{g} \tag{2}$$

The volume fraction $\alpha_d$ is defined as the ratio of the (fractional) volume of particle $i$ located in a computational cell $\Delta V_c$ while taking into account the total number of particles in a computational cell $k_c$.

$$\alpha_d = 1 - \sum_{i=1}^{k_c} \frac{V_i}{\Delta V_c} \tag{3}$$

The fluid viscous stress tensor $\tau$ for incompressible Newtonian fluid is given by Eq. (4), where $\delta_k$ is the Kronecker delta and $\mu$ is the viscosity. The fluid bulk viscosity is not considered in the present study as fluid compressibility is not considered. The particle-fluid interphasial force $\boldsymbol{F_{pf}}$ is given by Eq. (5). This volumetric particle-fluid interaction force comprises a myriad of solid-gas interaction forces, namely, the drag force, Saffman lift force, virtual mass force, Basset history force, and the pressure gradient force. The inclusion of the Saffman lift force, pressure gradient force, Basset term and virtual mass term showed negligible deviation in the dynamics of the system. This is usually the case for particle-fluid systems pertaining to small density ratios ($\rho_f/\rho_s \sim 10^{-3}$) (Afkhami et al., 2015; Hjelmfel and Mockros, 1966; Traore et al., 2015). The dominant force is the fluid drag force and gravity force. It is noteworthy that Eqs. (3) and (5) is applicable for both two- and three-dimensional conditions. For the two-dimensional cases presented in this study, a pseudo three-dimensional concept is employed (Xu and Yu, 1997).

$$\tau = -\frac{2}{3} \mu (\nabla \cdot \boldsymbol{v}) \delta_k + 2 \mu ((\nabla \boldsymbol{v}) + (\nabla \boldsymbol{v})^T) \tag{4}$$

$$\boldsymbol{F_{pf}} = \frac{1}{\Delta V_c} \sum_{i=1}^{k_c} \boldsymbol{f_{pf,i}} = \frac{1}{\Delta V_c} \sum_{i=1}^{k_c} (\boldsymbol{f_{d,i}}) \tag{5}$$

The transient interaction between the carrier phase and discrete phase is enabled in order to compute the total particle-fluid interaction force $\boldsymbol{F_{pf}}$ which explicitly takes into account all particle-fluid interaction forces exerted on a particle in a computational cell. The equations describing solid spherical particles is given by:

$$m_i \frac{dV_i}{dt} = m_i g + F_{CED} + \sum_{j=1}^{k_i} F_{C,ij} + f_{pf,i}, \tag{6}$$

where $V_i$ is the translational particle velocity and $m_i$ is the particle mass. The contact force $F_c$ between the particles and walls comprises the normal and tangential force; moreover, the damping force is related to the coefficient of restitution. The reader is referred to Tsuji et al. (1992) for the full description of the particle contacts. The cohesive force is given as $F_{CED}$, number of particles in contact with particle $i$ $k_i$, and the gravitational force $m_i g$. The angular momentum is given by Eq. (7) where $I_i$ is the moment of inertia, $T_i$ is the torque generated by the tangential forces, and $\omega_{pr}$ is the rotational velocity.

$$I_i \frac{d\omega_i}{dt} = \sum_{j=1}^{k_i} T_i \tag{7}$$

A soft-sphere discrete element method (DEM) based on a non-linear spring-slider-dashpot model (Cundall and Strack, 1979) is used to model the solid particles. Additionally, a linear cohesion model is introduced explicitly to account for the cohesive forces $F_{CED}$ between particle-particle and particle-wall contacts through the cohesion energy density (Fernandez and Nirschl, 2013). This adhesion force comprises the Van der Waals forces, electrostatic forces, and other inter-particle forces. The DEM method can capture the particle-particle and particle-wall interactions (four-way coupling) unlike the Eulerian-Lagrangian method which assumes zero particle volume. This coupled CFD-DEM method accounts for all cohesive particle-fluid $\boldsymbol{F_{pf}}$ interactions which is essential in particle-fluid systems. Particles $\rho_p$ = 500, 1500, 2500 kg/m³ of 50 μm diameter with a coefficient of restitution and coefficient of friction of 0.5 (Sauret and Hooman, 2014) is injected into the porous domain along the inlet plane. For the first time, a hybrid SIMPLE-PISO (PIMPLE) algorithm is deployed in the numerical studies pertaining to particle-laden gas flow in porous media to achieve numerical stability. A generalized geometric-algebraic multi-grid (GAMG) solver and a Gauss-Seidel smoother is used to obtain the discretized pressure equations while a smoother symmetric Gauss-Seidel (sGS) is used to obtain the discretized velocity equations. The DEM and CFD time-step is set to $10^{-5}$ s and $10^{-4}$ s respectively. Total simulation time is 1 s. The convergence criterion is set to $10^{-6}$ for the pressure residual and $10^{-5}$ for the velocity components residual. The particle injection rate is set to 250 particles per second (PPS), and particles are injected into the domain commencing 0.20 s. Therefore, a total of 200 particles are injected from 0.20 s to 1.00 s. To achieve stable momentum-pressure coupling, the following values are assigned to the PIMPLE control: 2 non-orthogonal correctors, 2 correctors, and 20 non-outer correctors, and a PIMPLE residual control. This coupled FVM-DEM code and the respective numerical schemes is developed and implemented in a C++ opensource CFD program called OpenFOAM which allows the end-user to customize and develop very advanced CFD algorithms. At the commencement of the simulation, both the particle solver (DEM) and fluid solver (FVM) is simultaneously executed. The data exchange at each time-step between the particle and fluid phase is realised by simultaneously executing both FVM and DEM solvers. The coupling between the two phases is achieved as follows: first, at each time-step, the DEM solver will relay the dynamic information such as positions and velocities of individual particles, in order to evaluate the porosity and the particle-fluid interaction force in a computational cell. Afterwards, the CFD solver will use this data to evaluate the gas flow field which computes the fluid forces acting on each DEM particle. Then all of these resultant forces are imported into the DEM in order to generate motion information of individual particles for the next time-step. The fluid force acting on each discrete particle will act in response on the carrier fluid from the DEM particles, thereby complying with Newton's third law of motion (Qian et al., 2014; Zhou et al., 2010).

### 2.2. Geometric configuration and boundary conditions

We consider laminar pore-level transport of particle-fluid flow in a porous channel flow with porosity ε of 92.92% as shown in Fig. 1. The idealized foam structure depicted in Fig. 1 is an approximate representation of the porosity of a real aluminium foam, sample No. 11 (Bhattacharya et al., 2002). Bhattacharya et al. (2002) enunciated that the results such as the friction factor of this idealized or approximate model align well with experimental data of real aluminium foams. It is noteworthy that Calmidi (1998) used an accurate representation of the real metal foam in the form of an idealized foam structure such as the one shown in Fig. 1. Hooman et al. (2012) and Tamayol and Hooman (2011) have used a very similar idealized theoretical model to Fig. 1 in the form of a cubic cell
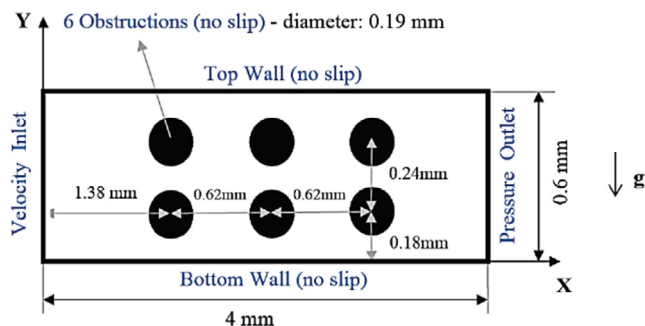
**Fig. 1.** Schematic of the computational domains (dimensions not to scale) and boundary conditions of the two idealized porous metal foams at the pore-level.

model, and it was found that the results, such as the effective heat transfer coefficient based on this simplified geometry, is in good agreement with experimental results based on real metal foam structures. Many other researchers have used a simplified repetitive cubic model as an alternative to a real metal foam structure as the latter is too computationally expensive and will yield computational complications (Dixit and Ghosh, 2016; Lu et al., 1998; Ghosh, 2008; Bhattacharya et al., 2002). Dixit and Ghosh (2016) concluded the idealized model is able to accurately explain the experimentally obtained temperature data. Therefore, the approximate model shown in Fig. 1 is used in this investigation. The existing computer capacity makes simulating particle-fluid flow, using this FVM-DEM method, at the macroscopic level within an idealized or a real metal foam geometry with hundreds of ligaments and pores (obtained via microtomography scans) extremely difficult and will lead to exorbitant computational costs which is the norm in fully resolved FVM-DEM or LBM-DEM methods. What is more, Zhu et al. (2007) enunciated the inherent difficulty in using these resolved methods for process modelling and control for very large and complex geometries. However, the accuracy of these methods make it suitable for fundamental research to particle technology/-physics (Zhu et al., 2007). Optimizing the numerics for very complex and larger 2D/3D geometries will be addressed in the near future.

Moreover, one of the main goals of this work is to quantify streamline behaviour; as such, we use 6 obstructions to represent the foam structure. This should be sufficient because the symmetric nature of the problem while retaining the realism of a solid-gas suspension. Secondly, quantifying streamline behaviour on a real foam is extremely complex. Thus, the geometry had to be reduced to an idealized configuration to mitigate this issue. The air velocity satisfies the no-slip boundary condition at the top wall and the foam ligaments. A no-slip boundary condition is enforced at the bottom wall in order to achieve a perceptible particle aggregate formation. The inlet velocity of the fluid $U_f$ is set to 0.10 m/s. A zero pressure

outlet is enforced. The geometry is built using ANSYS Designer Modeler (ANSYS v17, 2016) and the meshes are generated and solved in OpenFOAM (OpenFOAM v3.0.0, 2015). Post-processing of the results is achieved using ParaView (ParaView v4.1.0, 2014).

### 2.3. Mesh sensitivity analysis

The mesh elements of the entire geometrical object comprise of unstructured tetrahedral mesh elements. The mesh is refined around the vicinity of the circular ligaments. A mesh sensitivity analysis was performed using three different grids: 757 (Mesh 1), 1693 (Mesh 2), 2652 (Mesh 3) nodes. The mesh analysis is based on single-phase (fluid only) flow. The global pressure drop (difference between the maximum and minimum pressure values) based on three different grids are shown in Table 1. Mesh 2 is used for our simulation as the pressure drop discrepancy between Mesh 2 and Mesh 3 is significantly less 5%. A schematic of the mesh is shown in Fig. 2. A minimum orthogonal quality of 0.62 is registered. Although successive mesh refinements observe a maximum 5% pressure drop increase, the FVM-DEM framework does not permit the use of an extremely low mesh cell size to DEM particle size ratio as this will compromise solution accuracy and numerical stability. Laminar flow is considered in this study, and the pressure drop can be considered reasonably accurate. Thus, Mesh 2 is selected for the numerical investigation.

In the event of multiphase solid-gas flow, trial numerical results have shown that the particle distribution patterns, pressure drop profiles, and fluid velocity patterns are very similar regardless of the mesh size and the quality of the mesh. This is attributable to the simplicity of the geometric domain. Furthermore, a 1:1 mesh cell size to particle diameter ratio or higher is assigned to prevent any numerical instabilities whilst ensuring numerical accuracy (Kuruneru et al., 2016). In this study, the mesh cell size to particle diameter ratio is about 1.5:1. A maximum solid volume fraction approximation method is enforced to nullify numerical stability problems in the event a particle approaches the vicinity of an obstruction where the particle size slightly exceeds the mesh cell size; and the mass and momentum sources is distributed to neighbouring cells as a means to conserve mass and energy (Wahyudi et al., 2016). It is noteworthy that Wahyudi et al. (2016), Wang et al. (2012) and Zhou et al. (2016) have used very similar ratios and their numerical model has been successfully validated against experimental data. Additionally, the PIMPLE algorithm, which is beneficial for transient simulations (for example where the mesh cell size is only slightly larger than the DEM particle size) on unstructured skewed non-orthogonal meshes at acceptably high courant numbers, stabilises numerical convergence.

## 3. Results and discussion

### 3.1. Analytical and numerical pressure drop and particle distribution profiles

The transport of fluid through a porous medium comprises the viscous and inertial effect which is based on the Darcy-Forchheimer equation (Vafai, 1984):

**Table 1**
Pressure drop profiles for three different meshes.

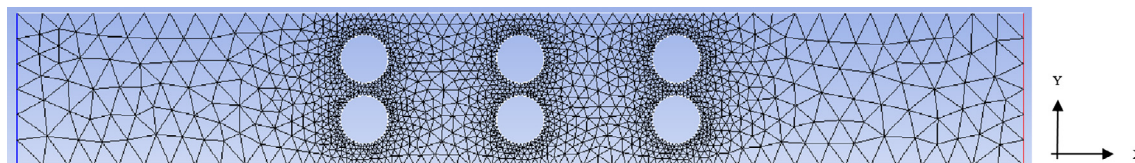| Mesh | Number of nodes $N$ (–) | Global pressure drop $\Delta P$ (Pa) |
|------|-------------------------|--------------------------------------|
| 1    | 757                     | 4.29                                 |
| 2    | 1693                    | 4.73                                 |
| 3    | 2652                    | 4.88                                 |



**Fig. 2.** Computational grid of a 6-pore configuration.

$$\Delta P = \frac{\mu_f}{K_F} U_f L_M + \frac{\rho_f F}{\sqrt{K_F}} U_f^2 L_M \tag{8}$$

$$c_1 = \frac{A}{36\kappa}, \quad K_F = \frac{K}{c_1}, \quad F = \frac{B}{6\varepsilon_m^{1.5}\sqrt{c_1}\sqrt{\kappa}} \tag{9}$$

where $K_F$ is the permeability in the Forchheimer regime, $F$ is the Forchheimer constant, $K$ is the permeability in the Darcy regime, $U_f$ is the superficial velocity of the fluid, and $L_M$ is the modified length of the packed porous channel or packed bed. The parameter A connotes the Ergun constant which is taken to be 150. The constant B depends on the particle roughness and is set to 1.75 for smooth particles as this value relates to smooth particles (Macdonald et al., 1979) which is considered in the present analysis. In this study, as time elapses, the accumulation of particle deposits in the porous metal foam alters the original porosity $\varepsilon$ (i.e. $\varepsilon \to \varepsilon_m$) and original length of the packed channel ($L \to L_M$). ImageJ software is used to quantify the magnitude of the modified porosity $\varepsilon_m$ and packed bed length $L_M$ of the clogged channel at different time intervals. To facilitate the calculation of the modified porosity $\varepsilon_m$ at various time points, ImageJ software is used to compute the area covered by the deposited particles at a particular time point. The permeability of a porous structure $K$ is evaluated based on the hydraulic radius theory of Kozeny Carman (Dukhan et al., 2014) and is given by:

$$K = \frac{\varepsilon_m^3 d_p^2}{36\kappa(1-\varepsilon_m)^2} \tag{10}$$

where $\kappa$ is the Kozeny-Carman factor (Happel and Brenner, 1973), $d_p$ is the particle diameter. In this study, the fluid Reynolds number is calculated as a function of the square root of the metal foam permeability $K$ as the characteristic length. Previous studies have shown that the original Darcy-Forcheimer equation (Eqs. (8) and (9)) miscalculates the pressure drop at very low Reynolds numbers ($O(0.1) < Re < O(10)$) (Sivanesapillai et al., 2014). Variants of this original equation and the Carman Kozeny equation are available depending on the application (Alazmi and Vafai, 2000; Rumpf and Gupte, 1971; Wu et al., 2008); clearly, the usage of the Darcy-

Forchheimer equation has deep theoretical and empirical arguments and has been a subject of debate.

According to Table 2, the numerical pressure drop increases with time signifying the gradual increase in particle deposition (D.F.) in the porous medium, which in turn alters the original porosity of the foam. The transient behaviour of solid-gas saturated foam is quantified by the pressure drop and porosity variation, shown in Fig. 3. A steady increase in the pressure drop is observed while a sharp decrease in porosity is observed from 0.40 s to 0.70 s. The deposition fraction is calculated as the ratio of the number of particles that have settled on the bottom wall, with zero particle velocity, to the total number of particles. Moreover, the numerical pressure drop values for $Re \geq 0.1$ ($\varepsilon_m \geq 80\%$) align well with the original Darcy-Forchheimer equation, thus lending credence to the present numerical procedure. However, minimum discrepancy is realised between the numerical pressure drop and the pressure drop obtained by the modified Darcy-Forchheimer equation given by:

$$\Delta P = 0.1 \frac{\mu_f}{K_F} U_f L_M + 0.1 \frac{\rho_f F}{\sqrt{K_F}} U_f^2 L_M \tag{11}$$

for $Re < 0.1$ ($\varepsilon_m < 80\%$). In addition, the large discrepancy between the original Darcy equation and the numerical pressure drop is attributable to the presence of highly irregular rectangular shaped particle aggregates from the inlet to the first column obstruction wall as shown in Fig. 4c. There is a scarcity of information in the literature pertaining to the validity of the Darcy-Brinkman-Forchheimer (DBF) equations for fluid flow past irregular porous structures for various Reynolds numbers.

Interestingly, Allen et al. (2013) concluded that the Darcy-Forchheimer equation underestimates the pressure drop in a packed bed of irregular shaped solid particles by a factor as high as 5. It was argued that the packing arrangement and shape have been at play in miscalculating the pressure drop. This highly irregular packing arrangement together with a low fluid Reynolds number at low porosities is arguably linked to the discrepancy of the pressure drop. A similar motif is discussed by Allen et al. (2013). A comparable observation is observed at 0.70 s and 1.00 s, as

**Table 2**
Comparative assessment between numerical and analytical pressure drop profiles.

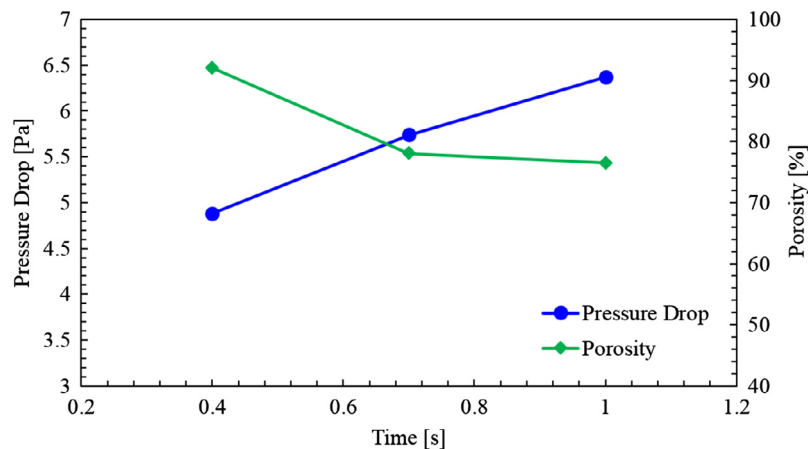| Time (s) | $\varepsilon_m\%$ | $\Gamma$ | Deposition fraction % | $\Delta P$ (Numerical) | $\Delta P$ (Eq. (8)) | $\Delta P$ (Eq. (11)) |
|---|---|---|---|---|---|---|
| 0.40 | 92.05 | 1.04 | 6.50 | 4.88 | 5.37 | 0.54 |
| 0.70 | 78.08 | 1.13 | 45.50 | 5.74 | 54.27 | 5.43 |
| 1.00 | 76.54 | 1.14 | 68.50 | 6.37 | 60.94 | 6.09 |



**Fig. 3.** Time evolution of pressure drop $\Delta P$ and porosity $\varepsilon_m$.
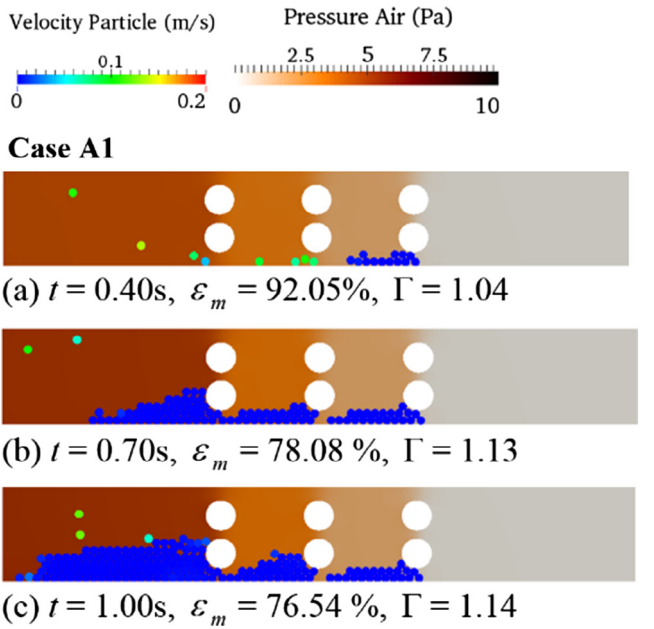
Fig. 4. Snapshots of particle-laden gas flows from 0.40 s to 1.00 s. Direction of flow from left to right.

shown in Table 2, where the original equation miscalculates the pressure drop by a factor as high as 10. It is worth noting that this trait is prevalent in the 6-pore configuration with very low Reynolds number ($Re < 0.1$) and low porosity $\varepsilon_m$. The fluid tortuosity $\Gamma$ is given as a function of the porosity $\varepsilon$ of a particular configuration as per the Bruggeman relation (Bruggeman, 1935):

$$\Gamma = \varepsilon_m^{-0.5} \qquad (12)$$

The existing literature on the permeability relationship (Eq. (10)) is invariably given as a function of the porosity. Hereinafter, a new form of the Carman-Kozeny equation between the permeability $K$ and the tortuosity of the fluid flow in porous media $\Gamma$ is proposed by harnessing the Bruggeman relation. So, substituting Eq. (12) into **10** yields:

$$K = \frac{(\Gamma^{-2})^3 d_p^2}{36\kappa(1 - \Gamma^{-2})^2} \qquad (13)$$

This new relation explicitly takes into account the meandering or waviness of the path in a porous media. This relationship shows that, for a constant particle diameter $d_p$ and Kozeny factor $\kappa$, as the modified porosity $\varepsilon_m$ decreases with time, the permeability $K$ decreases with increasing tortuosity of the fluid $\Gamma$, as shown in Table 2.

The transient evolution of particle-fluid gas flows and particle deposition from 0.40 s to 1.00 s is shown in Fig. 4. The original porosity $\varepsilon$ of the metal foam and pore-level fluid tortuosity $\Gamma$ varies with time due to the presence of deposits. Particles with a zero velocity infer an idle or deposited particle in the foam structure. The temporal development of particle aggregate height varies non-uniformly with elapsed time. Moreover, a 17.6% reduction of foam porosity $\varepsilon_m$ is realised at 1.00 s where the metal foam is partially clogged. Gravitational sedimentation is the primary mode of solid particle transport. As time elapses, particle deposits engulf the metal foam cylindrical ligaments, which artificially accentuates the ligament surface roughness. Particle-particle interactions become more profound as the number of deposited particles increase. Commencing approximately 0.70 s, the deposited particles have a strong influence on the motion of the fluid near the vicinity of the deposited particles, in particular from the inlet plane to the first column obstruction walls. Large swathes of deposited particles are located along the bottom wall from the inlet plane to the first row obstruction walls. The continuous accumulation of deposited particles results in a heightened pressure drop.

### 3.2. Unsteady particle-laden fluid and fluid flow analysis

Having concluded the numerical analysis of particle-fluid flow, particle deposition, and quantitative analysis of pressure drop, we now turn our attention to the shift in the position of the fluid streamlines. This is quantified by the tortuosity and the streamline angle, the latter of which will be explained in the subsequent paragraph. The computation of these two parameters provides an insight into the resistance to fluid flow and the tortuosity based on various foulant densities and fluid Reynolds number. Moreover,
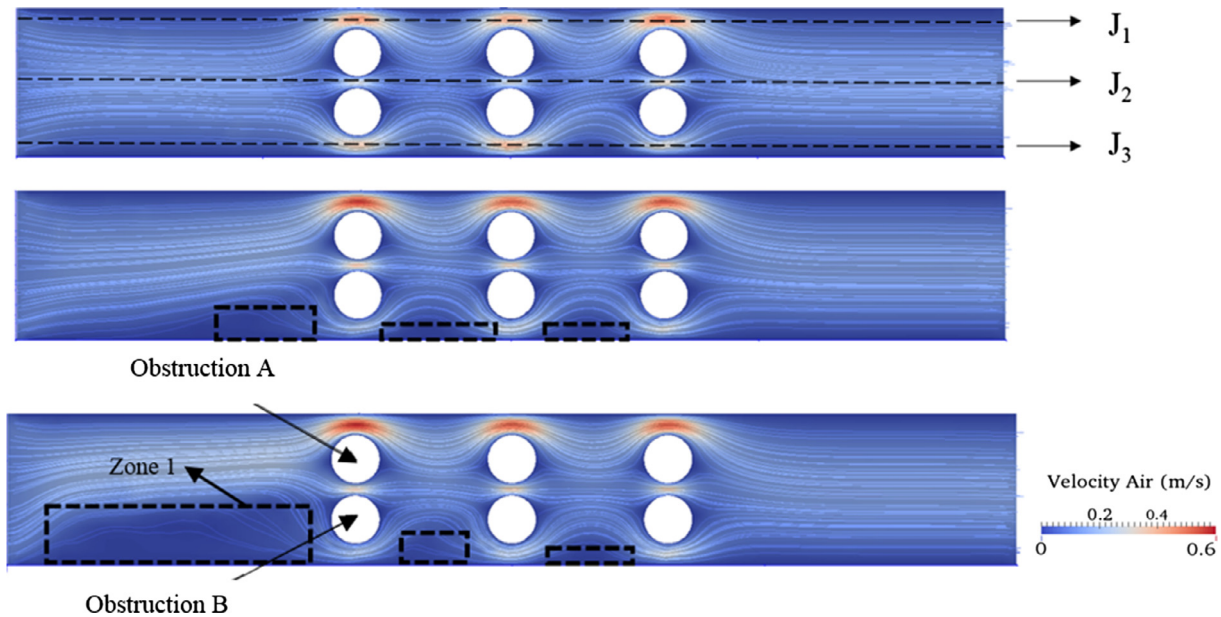


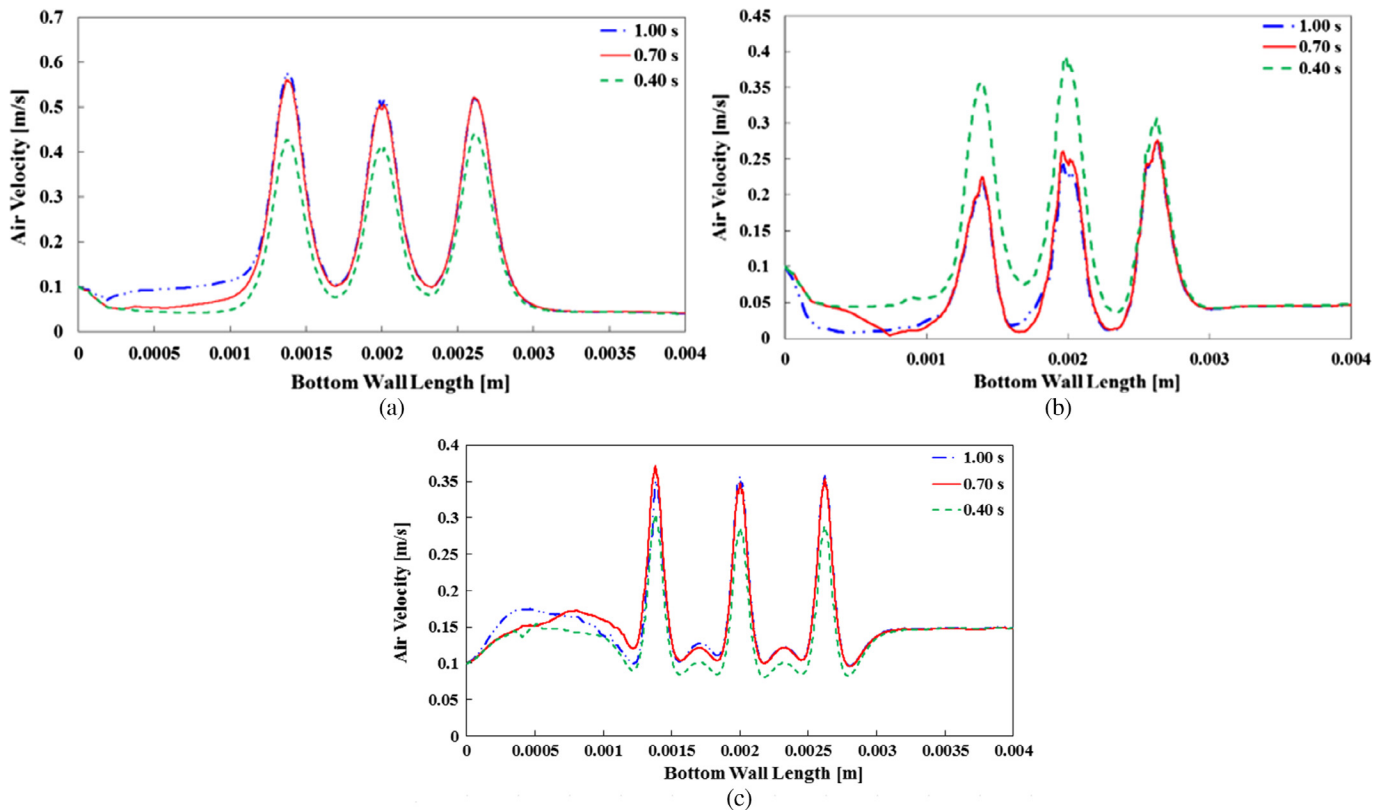Fig. 5. Fluid streamlines at 0.40 s (top) 0.70 s (middle) 1.00 s (bottom).

(a)



(b)



(c)

**Fig. 6.** Air velocity magnitudes along (a) $J_1$ (b) $J_3$ (c) $J_2$ at three time intervals.

the numerical values of the streamline angle and tortuosity values permit the calculation of permeability at any time point. The streamlines depicting bounded fluid flows are shown in Fig. 5. The direction of flow is from left to right. The solid particles have been deliberately removed for the sake of clarity. The dashed rectangles highlighted in Fig. 5 denote the location of deposited particles immersed in a quiescent fluid environment. As time elapses, the fluid void fraction decreases significantly and the disturbance in fluid streamlines, connoted by a substantial change in the fluid velocity profiles around obstructions A & B, is clearly observed in Fig. 5. Consequently, the maximum air velocity located above the obstruction A increases from 0.42 m/s at 0.40 s to 0.58 m/s at 1.00 s.

The magnitudes of air velocity along three separate regions are discerned by the dashed lines $J_1$, $J_2$, and $J_3$, as shown in Fig. 5. Fluid velocity profiles are extracted based on three different time intervals and presented in Fig. 6. The difference between the maximum air velocities between any two time intervals is highest at $J_3$. This is linked to the presence of deposits along the bottom wall. A close-up of the fluid streamlines and fluid velocity contours pertaining to obstruction surfaces A and B at 0.40 s and 1.00 s (Fig. 5) is illustrated in Fig. 7. Bubble layer separation was not observed in our simulations. An interesting observation is the change in the angle of the incoming streamline and the transient meandering of streamlines, which is denoted by a red[1] dashed line directed towards the point of stagnation on the obstruction surfaces A and B. This instantaneous shift will be assigned as the *streamline angle* $\Phi$ and the *change in the streamline angle* between the two time intervals is denoted as $\Upsilon$, namely:

$$\Upsilon_u = \Phi_{u,1} - \Phi_{u,2} \qquad (14)$$

where u is assigned as either obstruction A or B as shown in Fig. 7. A high $\Upsilon_u$ connotes a reduction in the original porosity from $\varepsilon$ to $\varepsilon_m$ of the configuration and change in tortuosity $\Gamma$ because of the presence of particle deposits. Consequently, the tortuosity of fluid flow, between regions $J_1$ and $J_2$, increases as shown in Fig. 7 (right). This alters the waviness $\Gamma$ of the porous media and decreases the permeability as per the newly derived Carman-Kozeny equation, given by Eq. (13). The magnitude of $\Upsilon_u$ is contingent on the bulk fluid viscosity, particle concentration density within the vicinity of the obstructions, and the solid particles' physical properties such as the porosity. A notable shift in the streamline angle is observed in obstruction B as a direct consequence of the presence of solid deposits along the bottom wall, which in turn alters the streamline angle around obstruction A.

The streamlines become progressively convergent as they approach the obstruction surface where a maximum fluid velocity is localized at the top of the obstruction surface A as shown in Fig. 7 (right). The streamline angle ratio $R_{SA}$ is defined as the ratio of the streamline angle of obstruction surface B to that of A at a given time. $R_{SA}$ has been calculated from 0.1 s to 1.0 s and is denoted by circular markers ($U_f = 0.10$ m/s) and cross markers ($U_f = 0.15$ m/s). According to Fig. 8a, the relationship between $R_{SA}$ and time t for the $U_f = 0.10$ m/s case is given as:

$$R_{SA} = 2.92t^2 - 1.30t + 1.09 \qquad (15)$$

Likewise, the streamline angle ratio is plotted against the fluid tortuosity based on a time interval 0.1–1.0 s as shown in Fig. 8b. We must emphasize that, at $U_f = 0.10$ m/s, the fluid tortuosities at 0.1 s, 0.2 s, and 0.3 s yield identical streamline angle ratio because a negligible change in the original porosity ($\varepsilon = \varepsilon_m$) is observed. From Fig. 8b, the relationship between $R_{SA}$ and $\Gamma$ at $U_f = 0.10$ m/s can be written as:

---

[1] For interpretation of color in Fig. 7, the reader is referred to the web version of this article.
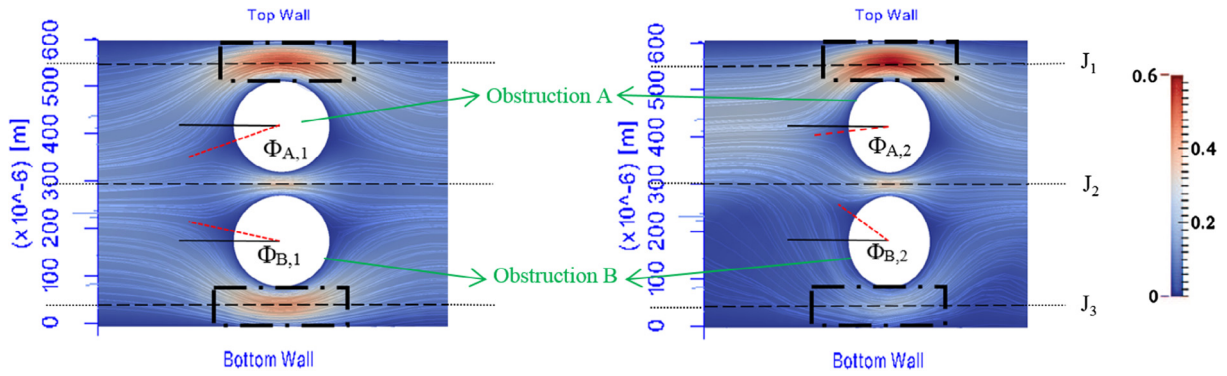
**Fig. 7.** Fluid velocity contours and variation in the streamline angle between 0.40 s (left) and 1.00 s (right) on the obstruction surfaces A and B.
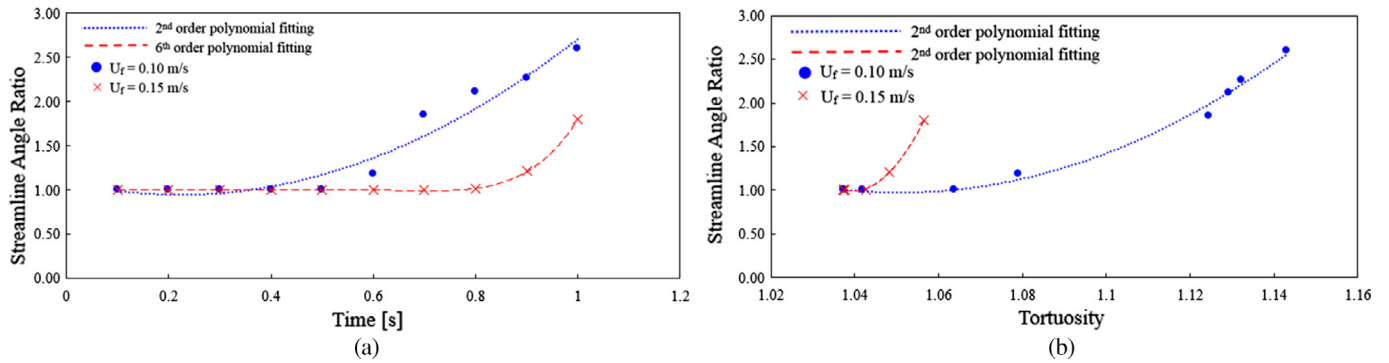


**Fig. 8.** Least squares fitting of (a) streamline angle ratio with time and (b) streamline angle ratio with tortuosity for two inlet velocities $U_f$ = 0.10 m/s and 0.15 m/s.

**Table 3**
Time evolution of streamline angles $R_{SA}$ and tortuosity $\Gamma$ for particle density.

| $U_f$ (m/s) | Time (s) | $R_{SA}^1$ | $\Gamma^1$ | $R_{SA}^2$ | $\Gamma^2$ | $R_{SA}^3$ | $\Gamma^3$ |
|---|---|---|---|---|---|---|---|
| 0.10 | 0.40 | 1.000 | 1.037 | 1.000 | 1.038 | 1.000 | 1.042 |
| 0.10 | 0.70 | 1.000 | 1.037 | 1.127 | 1.045 | 1.852 | 1.125 |
| 0.10 | 1.00 | 1.647 | 1.044 | 2.022 | 1.057 | 2.599 | 1.143 |
| 0.15 | 0.40 | 1.000 | 1.037 | 1.000 | 1.038 | 1.000 | 1.037 |
| 0.15 | 0.70 | 1.000 | 1.037 | 1.115 | 1.042 | 1.000 | 1.037 |
| 0.15 | 1.00 | 1.000 | 1.037 | 2.004 | 1.062 | 1.800 | 1.057 |

[1] $\rho_p$ = 500 kg/m³.
[2] $\rho_p$ = 1500 kg/m³.
[3] $\rho_p$ = 2500 kg/m³.

$$R_{SA} = 186.69\Gamma^2 - 392.40\Gamma + 207.17 \tag{16}$$

Utilizing Eqs. (15) and (16), an expression for the time dependent fluid tortuosity can be obtained as

$$2.92t^2 - 1.30t = 186.69\Gamma^2 - 392.40\Gamma + 206.08 \tag{17}$$

The streamline angle ratio $R_{SA}$ exhibits a monotonic behaviour with both time and pore-level fluid tortuosity as shown in Fig. 8 for both $U_f$ = 0.10 m/s and 0.15 m/s. At $U_f$ = 0.10 m/s, the tortuosity profile displays a quasi-steady behaviour from 0.10 s to 0.60 s, after which a sharp increase in the fluid tortuosity is observed from 0.6 s onwards.

The precipitous deviation from a quasi-steady behaviour for a Newtonian fluid at 0.6 s to a heightened change in streamline angle and fluid tortuosity signifies a high particle concentration density around an obstruction surface(s), for instance, zone 1 depicted in Fig. 5. The sharp increase in deposition fraction in zone 1 between 0.6 s and 0.8 s yields an acceleration effect of the fluid flow within

the vicinity of obstructions A and B, thereby generating a sharp rise in the streamline angle and maximum fluid velocity. According to Fig. 6a, at $U_f$ = 0.15 m/s, a higher particle deposition rate is realised commencing at 0.80 s and consequently shifting the streamline angle. Thus, the transient progression of particle deposition increases $R_{SA}$ and $\Gamma$, shown in Fig. 8. This episode decreases the permeability, according to Eq. (13), which is manifested by a high particle concentration. It should be noted that an $R_{SA}$ of 1 signifies no change in the position of the fluid streamlines, and a $\Gamma$ value of 1.037 corresponds to the tortuosity of the porous geometry without any deposited particles.

Interestingly, according to Table 3, our results show that for relatively lighter particles ($\rho_p$ = 1500 kg/m³), $R_{SA}$ and $\Gamma$ are unexpectedly similar for $U_f$ = 0.10 m/s and $U_f$ = 0.15 m/s even though a 9% variation in D.F. is registered. Our observations indicate that the frequency of collisions between particles and obstacles A & B are slightly higher for the 1500 kg/m³ particles than the 2500 kg/m³ particles, which in turn amplifies sedimentation and the amount

of deposition along the bottom wall from the inlet to obstacles A & B. This explains the near identical $R_{SA}$ and $\Gamma$ for the 1500 kg/m³ particles irrespective of $U_f$. The 500 kg/m³ particles exhibit a noticeable shift in $R_{SA}$ and $\Gamma$ commencing at about 0.85 s for $U_f = 0.10$ m/s which is sensibly identical to Fig. 8 for $\rho_p = 2500$ kg/m³ for $U_f = 0.15$ m/s, whereas the streamline angles remain invariant with time for $U_f = 0.15$ m/s. A critical $R_{SA}/\Gamma$ ratio exists for all cases shown in Table 3 where the deposited particles alter the position of the fluid streamlines. For example, the meandering of the fluid streamlines corresponds to a critical $R_{SA}/\Gamma$ ratio of 1.646 at 0.70 s for the case with $\rho_p = 2500$ kg/m³ for $U_f = 0.10$ m/s; conversely, although there exists a small amount of deposited particles at 0.40 s, the position of the fluid streamlines remained invariant. The invariance of $R_{SA}$ and $\Gamma$ with Reynolds number is confined for the intermediate particle-fluid density ratio at 1500 kg/m³. Interestingly, the result of this ratio along with the other two (500 kg/m³ and 2500 kg/m³) signifies that evaluating the maximum heat transfer coefficient would be very useful to quantify the potentially varying degrees of competition among particle-wall conduction and particle-fluid convection in porous media.

The $R_{SA}$ and $\Gamma$ values are used to characterize the resistance to fluid flow as a result of the constriction of both the geometry's circular ligaments and the blockage of these ligaments because of the accumulation of deposited particles. A heightened curvature $R_{SA}$ and $\Gamma$ connotes fluid resistance, in the form of a high pressure drop and increased waviness, caused by the clogging of the porous media by the discrete particles. These parameters serve as the basis for better optimizing various compact porous media heat exchanger applications such as foams, fins, tubular bundles, microchannels with ordered cylinder arrays, porous catalysts and electrodes by realigning or restructuring any porous media geometrical parameter such as the pore diameter, wall thickness, among others. The numerical values of tortuosity and streamline angle shown in Table 3, together with Eqs. (16) & (17) permit the computation of the foam permeability or fluid resistance (Eq. (13)) at any given time point. The results presented in Table 3, such as a variation in $R_{SA}$ and $\Gamma$, correlate to a change in fluid flow velocity and pressure drop variation. These results could be used for unravelling complex solid-gas behaviour in turbulent flows and deciphering the time evolution of tortuosity in porous structures using pore-level LES-DEM type simulations. The streamlines and its corresponding field variables such as $R_{SA}$ and $\Gamma$ could be used to visualize and understand various flow patterns in various porous media configurations based on various particle-fluid properties and Reynolds numbers. This could pave the way for deeper insight into the stability and transition of the wavy flow solid-gas or any other form of multiphase transport in porous media. The evaluation of the streamline angle ratio yields as estimate of the foam porosity, consequently giving the end-user information about the permeability. The existing literature lacks experimental studies on solid-gas flow in porous media. However, the present numerical results will serve as a steppingstone to advance existing single-phase transport laboratory experiments to account for multiphase transport. This could be accomplished with the use of an advanced particle image velocimetry (PIV) technique. This technique will decipher the various mechanisms governing the mixing of materials of two or more phases at a various Reynolds numbers.

## 4. Conclusion

A coupled FVM-DEM method is developed to examine pore-level particle-fluid transport and the evolution of tortuosity of an idealized porous metal foam structure. A new time-dependent pore level fluid tortuosity relationship together with a modified porosity-based Darcy-Forchheimer analytical equation is devel-oped. The numerical pressure drop values for $\varepsilon_m \geq 80\%$ align well with the analytical pressure drop values obtained from the Darcy-Forchheimer equation whereas the modified Darcy-Forchheimer equation aligned well with numerical pressure drop values for $50\% \leq \varepsilon_m < 80\%$. Particle deposition alters fluid flow behaviour ($R_{SA}$), augments tortuosity $\Gamma$, and decreases the permeability as per the newly derived Carman-Kozeny relation. It is observed that the tortuosity is dependent on the solid-gas physical properties and flow Reynolds number. The streamline angle and tortuosity results provide an insight into the dynamical evolution of the solid-gas interactions, fluid flow patterns, and the permeability or resistance to fluid flow in the presence of a secondary phase. The results, together with the deployed numerical method, will serve as a steppingstone to optimize porous media geometrical configurations for the purposes of heat transfer enhancement, fluid mixing, and fouling alleviation. It could provide insight into the non-isothermal particle-fluid mixing in porous media at various Reynolds numbers. Moreover, this investigation could serve as the basis for examining unsteady multiphase transport in variable porosity media (Alazmi and Vafai, 2000). Further research is warranted to optimize the numerics for macro-scale simulations of particle-fluid flow such as particle clustering and turbophoresis. The numerics could be used and further developed to extend various chemical engineering studies such as bubbling fluidized beds, gas-solid slurry transport, transport of solid-gas and reactants, fixed-bed reactors, and biomass gasification.

## References

Afkhami, M., Hassanpour, A., Fairweather, M., Njobuenwu, D.O., 2015. Fully coupled LES-DEM of particle interaction and agglomeration in a turbulent channel flow. Comput. Chem. Eng. 78, 24–38.

Ahmed, J., Pham-Huu, C., Edouard, D., 2011. A predictive model based on tortuosity for pressure drop estimation in 'slim' and 'fat' foams. Chem. Eng. Sci. 66 (20), 4771–4779.

Alazmi, B., Vafai, K., 2000. Analysis of variants within the porous media transport models. J. Heat Transfer 122, 303–326.

Allen, K.G., von Backström, T.W., Kröger, D.G., 2013. Packed bed pressure drop dependence on particle shape, size distribution, packing arrangement and roughness. Powder Tech. 246, 590–600.

ANSYS ® Academic Research, Release 17.2, 2016.

Balakin, B.V., Hoffmann, A.C., Kosinski, P., 2011. Experimental study and computational fluid dynamics modeling of deposition of hydrate particles in a pipeline with turbulent water flow. Chem. Eng. Sci. 66 (4), 755–765.

Balakin, B., Lo, S., Kosinski, P., Hoffmann, A., 2016. Modelling agglomeration and deposition of gas hydrates in industrial pipelines with combined CFD-PBM technique. Chem. Eng. Sci. 153, 45–57.

Bayomy, A., Saghir, M., Yousefi, T., 2016. Electronic cooling using water flow in aluminum metal foam heat sink: experimental and numerical approach. Int. J. Therm. Sci. 109, 182–200.

Bhattacharya, A., Calmidi, V.V., Mahajan, R.L., 2002. Thermophysical properties of high porosity metal foams. Int. J. Heat Mass Transf. 45, 1017–1031.

Bruggeman, D.A.G., 1935. Berechnung verschiedener physikalischer konstanten von heterogenen substanzen. Ann. Phy 24, 636–679.

Carman, P.C., 1956. Flow of Gases Through Porous Media. Butterworths Scientific Publications, London.

Calmidi, V.V., 1998. Transport phenomena in high porosity metal foams PhD Thesis. University of Colorado, Boulder, CO.

Chen, X., Tavakkoli, F., Vafai, K., 2015. Analysis and characterization of metal foam-filled double-pipe heat exchangers. Numer. Heat Transf., Part A: Appl. 68 (10), 1031–1049.

Coletti, F., Muramatsu, K., Schiavazzi, D., Elkins, C., Eaton, J., 2014. Fluid flow and scalar transport through porous fins. Phys. Fluids 26, 55104.

Cundall, P.A., Strack, O.D., 1979. A discrete numerical model for granular assemblies. Geotechnique 21, 47–65.

Dixit, T., Ghosh, I., 2016. An experimental study on open cell metal foam as extended heat transfer surface. Exp. Thermal Fluid Sci. 77, 28–37.

Dritselis, C.D., 2017. Numerical study of particle deposition in a turbulent channel flow with transverse roughness elements on one wall. Int. J. Multiph. Flow 91, 1–18.

Dukhan, N., 2012. Analysis of brinkman-extended Darcy flow in porous media and experimental verification using metal foam. J. Fluids Eng., Trans. Am. Soc. Mech. Eng. 134, 71201.

Dukhan, N., Bagci, O., Ozdemir, M., 2014. Experimental flow in various porous media and reconciliation of Forchheimer and Ergun relations. Exp. Therm. Fluid Sci. 57, 425–433.

Eaton, J.K., 2009. Two-way coupled turbulence simulations of gas-particle flows using point-particle tracking. Int. J. Multiph. Flow 35 (9), 792–800.

Fernandes, C.S., Dias, R.P., Nóbrega, J.M., Maia, J.M., 2007. Laminar flow in chevron-type plate heat exchangers: CFD analysis of tortuosity, shape factor and friction factor. Chem. Eng. Process. 46 (9), 825–833.

Fernandez, X.R., Nirschl, H., 2013. Simulation of particles and sediment behaviour in centrifugal field by coupling CFD and DEM. Chem. Eng. Sci. 94, 7–19.

Giani, L., Groppi, G., Tronconi, E., 2005. Mass-transfer characterization of metallic foams as supports for structured catalysts. Ind. Eng. Chem. Res. 44 (14), 4993–5002.

Ghanbarian, B., Hunt, A.G., Ewing, R.P., Sahimi, M., 2013. Tortuosity in porous media: a critical review. Soil Sci. Soc. Am. J. 77 (5), 1461–1477.

Ghosh, I., 2008. Heat-transfer analysis of high porosity open-cell metal foam. J. Heat Transfer 130 (3), 34501.

Han, Y., Cundall, P.A., 2013. LBM–DEM modeling of fluid–solid interaction in porous media. Int. J. Numer. Anal. Meth. Geomech. 37 (10), 1391–1407.

Han, X., Wang, Q., Park, Y., T'Joen, C., Sommers, A., Jacobi, A., 2012. A review of metal foam and metal matrix composites for heat exchangers and heat sinks. Heat Transfer Eng. 33 (12), 991–1009.

Happel, J., Brenner, H., 1973. Low Reynolds Number Hydrodynamics. Martinus Nijhoff, The Hague.

Hjelmfel, A.T., Mockros, L.F., 1966. Motion of discrete particles in a turbulent fluid. Appl. Sci. Res. 16 (2), 149–161.

Hooman, K., Tamayol, A., Malayeri, M.R., 2012. Impact of particulate deposition on the thermos-hydraulic performance of metal foam heat exchangers: a simplified theoretical model. J. Heat Transfer 134 (9), 92601.

Hutter, C., Büchi, D., Zuber, V., Rudolf von Rohr, P., 2011. Heat transfer in metal foams and designed porous media. Chem. Eng. Sci. 66 (17), 3806–3814.

Kopanidis, A., Theodorakakos, A., Gavaises, E., Bouris, D., 2010. 3D numerical simulation of flow and conjugate heat transfer through a pore scale model of high porosity open cell metal foam. Int. J. Heat Mass Transf. 53, 2539–2550.

Kuruneru, S.T.W., Sauret, E., Saha, S.C., Gu, Y.T., 2016. Numerical investigation of the temporal evolution of particulate fouling in metal foams for air-cooled heat exchangers. Appl. Energy 184, 531–547.

Kruger, T., Kusumaatmaja, H., Silva, G., Krüger, T., Shardt, O., Kuzmin, A., Viggen, E. M., 2017. The Lattice Boltzmann Method: Principles and Practice. Springer International Publishing, Switzerland.

Lanfrey, P., Kuzeljevic, Z.V., Dudukovic, M.P., 2010. Tortuosity model for fixed beds randomly packed with identical particles. Chem. Eng. Sci. 65 (5), 1891–1896.

Lee, L., Quek, T., Deng, R., Ray, M., Wang, C., 2004. Pneumatic transport of granular materials through a 90 degrees bend. Chem. Eng. Sci. 59 (21), 4637–4651.

Leonardi, C.R., McCullough, J.W.S., Jones, B.D., Williams, J.R., 2016–2015. Electromagnetic excitation of particle suspensions in hydraulic fractures using a coupled lattice Boltzmann-discrete element model. Comput. Particle Mech. 3 (2), 125–140.

Leonardi, Christopher R., Jones, Bruce D., Holmes, David W., Williams, John R., 2013. Simulation of complex particle suspensions using coupled lattice Boltzmann-discrete element methods. In: Proceedings of the 6th International Conference on Discrete Element Methods. From: DEM6: 6th International Conference on Discrete Element Methods, 5–6 August 2013, Golden, CO, USA.

Lu, T.J., Stone, H.A., Ashby, M.F., 1998. Heat transfer in open-cell metal foams. Acta Mater. 46 (10), 3619–3635.

Lu, B., Wang, W., Li, J., 2011. Eulerian simulation of gas–solid flows with particles of Geldart groups A, B and D using EMMS-based meso-scale model. Chem. Eng. Sci. 66 (20), 4624–4635.

Macdonald, I.F., El-Sayed, M.S., Mow, K., Dullien, F.A., 1979. Flow through porous media-the Ergun equation revisited. Ind. Eng. Chem. Fundam. 18 (3), 199–208.

MacMullin, R.B., Muccini, G.A., 1956. Characteristics of porous beds and structures. Am. Inst. Chem. Eng. J. 2 (3), 393–403.

Mancin, S., Zilio, C., Diani, A., Rossetto, L., 2012. Experimental air heat transfer and pressure drop through copper foams. Exp. Thermal Fluid Sci. 36, 224–232.

Marshall, J.S., 2009. Discrete-element modeling of particulate aerosol flows. J. Comput. Phys. 228 (5), 1541–1561.

Matsumura, Y., Jenne, D., Jackson, T., 2015. Numerical simulation of fluid flow through random packs of ellipses. Phys. Fluids 27, 23301.

Midoux, N., Charpentier, J.C., 1973. Apparent diffusivity and tortuosity in a liquid-filled porous catalyst used for hydrodesulfuration of petroleum products. Chem. Eng. Sci. 28, 2108.

Narsilio, G.A., Buzzi, O., Fityus, S., Yun, S.T., Smith, D.W., 2009. Upscaling of Navier Stokes equations in porous media: theoretical, numerical and experimental approach. Comput. Geotech. 36, 1200–1206.

Ni, P., Jonsson, L., Ersson, M., Jonsson, P., 2014. On the deposition of particles in liquid metals onto vertical ceramic walls. Int. J. Multiph. Flow 62, 152–160.

Onstad, A.J., Elkins, C.J., Medina, F., Wicker, R.B., Eaton, J.K., 2011. Full-field measurements of flow through a scaled metal foam replica. Exp. Fluids 50, 1571–1585.

OpenFOAM v3.0.0, 2015. <https://openfoam.org/release/3-0-0/>.

ParaView v4.1.0, 2014. <https://blog.kitware.com/paraview-4-1-0-available-for-download/>.

Qian, F., Huang, N., Lu, J., Han, Y., 2014. CFD-DEM simulation of the filtration performance for fibrous media based on the mimic structure. Comput. Chem. Eng. 71, 478–488.

Rad, S.E., Afshin, H., Farhanieh, B., 2015. Heat transfer enhancement in shell-and-tube heat exchangers using porous media. Heat Transfer Eng. 36 (3), 262–277.

Rumpf, H., Gupte, A.R., 1971. Einflusse der porositat und korngrobenverteilung im widerstandsgesetz der porenstromung. Chem. Ing. Tec. 43, 367–375.

Sauret, E., Hooman, K., 2014. Particle size distribution effects on preferential deposition areas in metal foam wrapped tube bundle. Int. J. Heat Mass Transf. 79, 905–915.

Sivanesapillai, R., Steeb, H., Hartmaier, A., 2014. Transition of effective hydraulic properties from low to high reynolds number flow in porous media. Geophys. Res. Lett. 41, 4920–4928.

Tamayol, A., Hooman, K., 2011. Thermal assessment of forced convection through metal foam heat exchangers. J. Heat Transfer 133 (11).

Tian, Z.F., Tu, J.Y., Yeoh, G.H., 2007. Numerical modelling and validation of gas-particle flow in an in-line tube bank. Comput. Chem. Eng. 31 (9), 1064–1072.

T'Joen, C., De Jaeger, P., Huisseune, H., Van Herzeele, S., Vorst, N., De Paepe, M., 2010. Thermo-hydraulic study of a single row heat exchanger consisting of metal foam covered round tubes. Int. J. Heat Mass Transf. 53 (15), 3262–3274.

Tong, Z., He, Y., 2015. A unified coupling scheme between lattice Boltzmann method and finite volume method for unsteady fluid flow and heat transfer. Int. J. Heat Mass Transf. 80, 812–824.

Thorat, I.V., Stephenson, D.E., Zacharias, N.A., Zaghib, K., Harb, J.N., Wheeler, D.R., 2009. Quantifying tortuosity in porous li-ion battery materials. J. Power Sources 188 (2), 592–600.

Traore, P., Laurentie, J., Dascalescu, L., 2015. An efficient 4 way coupling CFD-DEM model for dense gas-solid particulate flows simulations. Comput. Fluids 113, 65–76.

Tryggvason, G., 2010. Virtual motion of real particles. J. Fluid Mech. 650, 1–4.

Tsuji, Y., Tanaka, T., Ishida, T., 1992. Lagrangian numerical simulation of plug flow of cohesionless particles in a horizontal pipe. Powder Technol. 71 (3), 239–250.

Vafai, K., 1984. Convective flow and heat transfer in variable porosity media. J. Fluid Mech. 147, 233–259.

Vepsalainen, A., Shah, S., Ritvanen, J., Hyppanen, T., 2014. Interphase mass transfer coefficient in fluidized bed combustion by Eulerian CFD modeling. Chem. Eng. Sci. 106, 30–38.

Wahyudi, H., Chu, K., Yu, A., 2016. 3D particle-scale modeling of gas-solids flow and heat transfer in fluidized beds with an immersed tube. Int. J. Heat Mass Transf. 97, 521–537.

Wang, S., Guo, S., Gao, J., Lan, X., Dong, Q., Li, X., 2012. Simulation of flow behaviour of liquid and particles in a liquid-solid fluidized bed. Powder Technol. 224, 365–373.

Wu, J., Yu, B., Yun, M., 2008. A resistance model for flow through porous media. Transp. Porous Media 71, 331–343.

Xu, B.H., Yu, A.B., 1997. Numerical simulation of the gas-solid flow in a fluidized bed by combining discrete particle method with computational fluid dynamics. J. Fluid Mech. 52, 2785–2809.

Yang, C., Nakayama, A., Liu, W., 2012. Heat transfer performance assessment for forced convection in a tube partially filled with a porous medium. Int. J. Therm. Sci. 54, 98–108.

Yao, J., Fairweather, M., 2012. Particle deposition in turbulent duct flows. Chem. Eng. Sci. 84, 781–800.

Yusuf, R., Halvorsen, B., Melaaen, M.C., 2011. Eulerian-Eulerian simulation of heat transfer between a gas–solid fluidized bed and an immersed tube-bank with horizontal tubes. Chem. Eng. Sci. 66 (8), 1550–1564.

Zafari, M., Panjepour, M., Meratian, M., 2015. Microtomography-based numerical simulation of fluid flow and heat transfer in open cell metal foams. Appl. Therm. Eng. 80, 347–354.

Zeiser, T., 2002. Analysis of the flow field and pressure drop in fixed-bed reactors with the help of lattice Boltzmann simulations. Phys. Eng. Sci. 360 (1792), 507–520.

Zhang, J., Li, B., Huang, W., Lei, Y., He, Y., Tao, W., 2009. Experimental performance comparison of shell-side heat transfer for shell-and-tube heat exchangers with middle-overlapped helical baffles and segmental baffles. Chem. Eng. Sci. 64 (8), 1643–1653.

Zhong, W., Yu, A., Zhou, G., Xie, J., Zhang, H., 2016. CFD simulation of dense particulate reaction system: approaches, recent advances and applications. Chem. Eng. Sci. 140, 16–43.

Zhou, J., Du, C., Liu, S., Liu, Y., 2016. Comparison of three types of swirling generators in coarse particle pneumatic conveying using CFD-DEM simulation. Powder Technol. 301, 1309–1320.

Zhou, Z.Y., Kuang, S.B., Chu, K.W., Yu, A.B., 2010. Discrete particle simulation of particle-fluid flow: model formulations and their applicability. J. Fluid Mech. 661, 482–510.

Zhu, H.P., Zhou, Z.Y., Yang, R.Y., Yu, A.B., 2007. Discrete particle simulation of particulate systems: theoretical developments. Chem. Eng. Sci. 62 (13), 3378–3396.